Joule

CellPress

Article

Microfaceting: A new logic for hot-carrier energy harvesting in hybrid plasmonic nanostructures

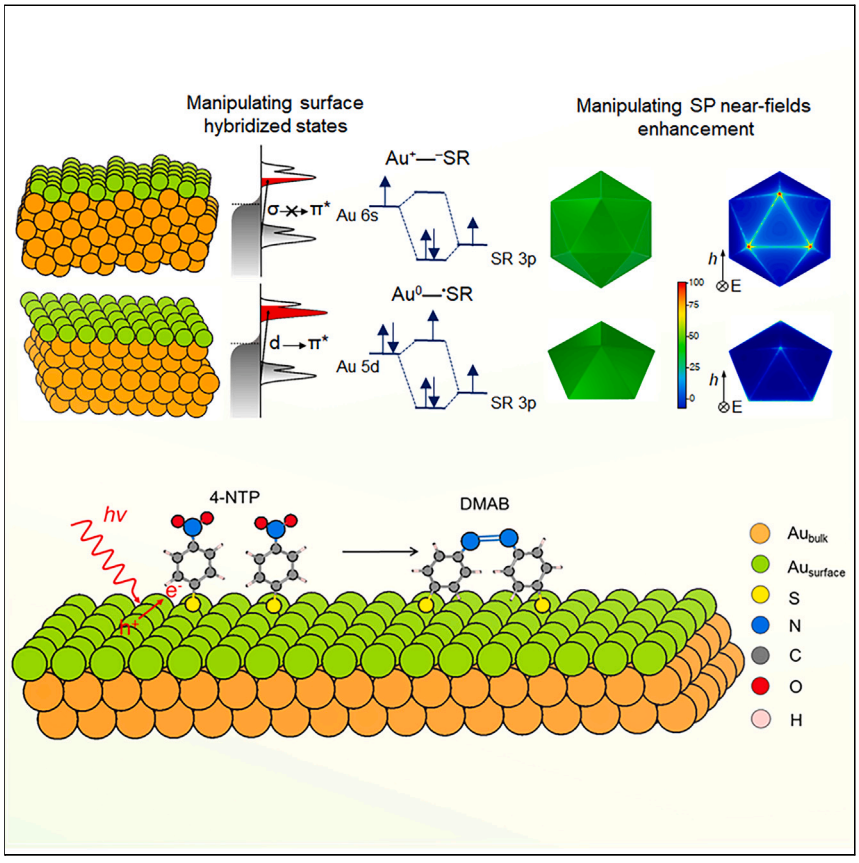

This work presents a novel strategy utilizing microfaceting, provides a comprehensive understanding of the microstructural and geometric effects of plasmonic nanostructures, and offers mechanistic insights into hot-carrier-driven photochemical surface reactions. It contributes to pushing forward the frontiers of plasmonic research from geometric control to nanostructure engineering and enlightens new strategies for diverse plasmonic-enhanced applications.

Wei Shao, Xiaoqiu Xu, Wenjing Zheng, ..., Jia Zhao, Xiaonian Li, Yihan Zhu

xnli@zjut.edu.cn (X.L.)
yihanzhu@zjut.edu.cn (Y.Z.)

Highlights

Microfaceting serves as a new logic for energy harvesting over hybrid plasmonic nanostructures

Decoupling microstructural and geometric effects in plasmonic photocatalysis

Mechanistic insights into interfacial state manipulation and hot-carrier-driven events

Shao et al., Joule 8, 141–156
January 17, 2024
https://doi.org/10.1016/j.joule.2023.11.004

Joule

CellPress

Article

Microfaceting: A new logic for hot-carrier energy harvesting in hybrid plasmonic nanostructures

Wei Shao,[1,8] Xiaoqiu Xu,[1,5,8] Wenjing Zheng,[1] Zhi Wang,[1] Qianqian Pan,[6] Xuelu Liu,[2] Weijian Tao,[3] Fanxin Liu,[4] Chongzhi Zhu,[1] Ping-Heng Tan,[2] Haiming Zhu,[3] Huijun Song,[1] Yu Han,[7] Tulai Sun,[1] Jia Zhao,[1] Xiaonian Li,[1,*] and Yihan Zhu[1,9,*]

SUMMARY

At the core of plasmonic-enhanced applications lies photon energy harvesting and conversion over plasmonic/non-plasmonic multicomponent hybrid materials. The direct excitation of local interfacial electronic states that arise from the chemical bonding between plasmonic metal and attached functional entity opens up an exceptionally efficient energy transfer channel. However, there is a lack of a general strategy to manipulate these states and insights into the impact of such electronic modulations on light-driven functionalities. We demonstrate in a plasmonic-metal/molecule hybrid system that by precisely manipulating microfacets of nanostructures, it is possible to engineer metal-adsorbate-hybridized interfacial states in terms of both energy gap opening and permissible electronic excitations. Low-index microfacets feature much more efficient interfacial electronic transitions than high-index ones, retarding plasmonic relaxation and entailing enhanced photocatalytic activity toward molecular coupling reactions. This study contributes to pushing forward frontiers of plasmonic research from geometric control to nanostructure engineering and enlightens new strategies for plasmonic-enhanced applications.

INTRODUCTION

Plasmonic nanostructures feature collective oscillations of free charge carriers upon resonant interactions with photons, which exhibit large optical cross-sections and allow the confinement of light energy at the surface.[1–5] The energy is dissipated through the formation of energetic charge carriers (i.e., "hot carriers") within the nanostructure that are sequentially involved in electron-electron scattering, electron-phonon (e-ph) scattering, and, finally, thermal equilibration with the environment at different time scales, spanning from hundreds of femtoseconds to a few picoseconds to hundreds of picoseconds, respectively.[6,7] The plasmon-induced thermalization leads to the heating of nanostructure and diverse photothermal applications like photothermal therapy and photothermal microscopy.[8,9] On the other side, plasmon-induced electric field leads to the increased optical scattering rates of nearby molecules and diverse plasmon-enhanced optical applications such as surface-enhanced Raman spectroscopy (SERS) and plasmon-enhanced fluorescence sensing.[10–13]

A more exciting emerging field that goes beyond the above-mentioned applications associated with bare plasmonic nanostructures focuses on the extraction of confined photon energy within a plasmonic nanostructure across an interface formed with

CONTEXT & SCALE

An exciting emerging field involves extracting photon energy in a hybrid plasmonic nanostructure across an interface, converting it into other energy forms like chemical and electrical energies. However, a fundamental understanding of the design rationale and the underlying logic behind hybrid plasmonic heterostructuring, as well as a general strategy to manipulate the efficiency of hot-carrier generation, transfer, and utilization at the microscale or even atomic level, is currently lacking. To address this gap, we propose a new logic for hot-carrier energy harvesting in a plasmonic-metal/molecule hybrid system through microfaceting. It enables us to engineer metal-adsorbate-hybridized interfacial states in terms of both energy gap opening and permissible electronic excitations. This study contributes to pushing the frontiers of plasmonic research from geometric control toward nanostructure engineering and sheds light on new strategies for diverse plasmonic-enhanced applications.

another non-plasmonic entity in terms of hot-carrier flow and the conversion of the energy flow into other energy forms like chemical and electrical energies.[14–16] These processes are achieved by photocatalysis and photovoltaics over the hybrid plasmonic nanostructure consisting of a plasmonic component that performs as a light absorber and a chemically attached non-plasmonic component that performs as an energy converter.[6,17] Typical hybrid plasmonic nanostructures may include plasmonic-metal/metal,[18] plasmonic-metal/semiconductor,[19] and plasmonic-metal/molecule systems.[20] In these systems, a quite small population of plasmon-excited hot-charge carriers that attain sufficient energy may be able to transfer from the metallic component to the chemically attached component with functionality before thermalizing to equilibrium, which is conventionally regarded as an indirect hot-carrier transfer mechanism.[21–23] This mechanism applies in hybrid plasmonic nanostructures composed of weakly bonded plasmonic and non-plasmonic entities like supported-Au/H_2 plasmon-enhanced photocatalytic systems (e.g., Au/TiO_2 and Au/SiO_2).[24] It has been reported in these systems that by exciting the surface plasmon (SP) of metallic component, the hot electrons locating at the high-energy tail of the nonequilibrium Fermi-Dirac distribution formed after dephasing would transfer to the antibonding states of adsorbed H_2 molecules and lead to the formation of metastable transient negative ion (TNI), $H_2^{\delta-}$.[25] The repetitive formation of TNIs allows the energy accumulation through vibrationally excited states and finally dissociates the H–H bonds.[25] Alternatively, for strongly bonded plasmonic and non-plasmonic entities with covalent bonds formed across their interface, the strong interfacial hybridization creates local electronic states that open up an energy gap and enable the direct momentum conserved excitations.[26] The resonant and direct charge transfer from populated hybridized states located at the plasmonic component to unpopulated states located at the non-plasmonic component provides an additional plasmon dephasing channel, namely chemical interface damping (CID), to more efficiently dissipate the electromagnetic energy.[27–29] The presence of such a direct interfacial charge transfer mechanism can be straightforwardly proved in plasmonic-metal/molecule hybrid systems (e.g., Ag-dye and Au-thiol systems[20,30]) by measuring the steady-state nonthermalized vibrational heating of chemisorbed molecules using anti-Stokes and Stokes Raman spectroscopy. The molecular vibrational temperature elevation as a result of charge transfer becomes dominant at the off-resonant wavelength of plasmonic metal (close to the resonant condition of metal-adsorbate-hybridized electronic states), corroborating the direct excitation of interfacial electronic states.[31] The chemically attached non-plasmonic entities also dramatically alter the plasmon decay dynamics of the metallic component in return, which can be investigated by using transient absorption (TA) pump-probe spectroscopy. It has been widely reported that interfacial states open up a faster energy dissipation channel in plasmonic-metal/semiconductor hybrid systems in contrast to bare plasmonic metal nanostructures.[32,33] Notwithstanding this, in plasmonic-metal/molecule hybrid systems, the hot adsorbate vibrationally excited through direct interfacial charge transfer may act as transient energy reservoirs of plasmon energy and significantly retards the overall thermalization process.[34,35] The relaxation time is tunable and also related with overall electronic heat capacity of the hybrid system.[36] In general, hybrid plasmonic nanostructures potentially provide a more efficient photon energy harvesting platform that enables the extraction of hot-carrier energy flow across the plasmonic/non-plasmonic interface.[26,37] Over these hybrid nanostructures, the majority of the photon energy is locally dissipated across the plasmonic/non-plasmonic interface,[38] which entails the fact that instead of geometric and shape regulation, the precise control and elucidation of nanoscopic interfacial structure are now the critical factors for designing and developing high-performance hybrid plasmonic nanostructures.

[1]Center for Electron Microscopy, Institute for Frontier and Interdisciplinary Sciences, State Key Laboratory Breeding Base of Green Chemistry Synthesis Technology and College of Chemical Engineering, Zhejiang University of Technology, Hangzhou, Zhejiang 310014, China

[2]State Key Laboratory of Superlattices and Microstructures, Institute of Semiconductors, Chinese Academy of Sciences, Beijing 100083, China

[3]Centre for Chemistry of High-Performance and Novel Materials, Department of Chemistry, Zhejiang University, Hangzhou, Zhejiang 310027, China

[4]Department of Applied Physics, Zhejiang University of Technology, Hangzhou, Zhejiang 310023, China

[5]Zhejiang Provincial Key Laboratory of Quantum Precision Measurement, College of Science, Zhejiang University of Technology, Hangzhou, Zhejiang 310023, China

[6]Engineering Research Center of Recycling & Comprehensive Utilization of Pharmaceutical and Chemical Waste of Zhejiang Province, Taizhou University, Taizhou, Zhejiang 318000, China

[7]Advanced Membranes and Porous Materials Center, Physical Science and Engineering Division, King Abdullah University of Science and Technology, Thuwal 23955-6900, Saudi Arabia

[8]These authors contributed equally

[9]Lead contact

*Correspondence: xnli@zjut.edu.cn (X.L.), yihanzhu@zjut.edu.cn (Y.Z.)

https://doi.org/10.1016/j.joule.2023.11.004

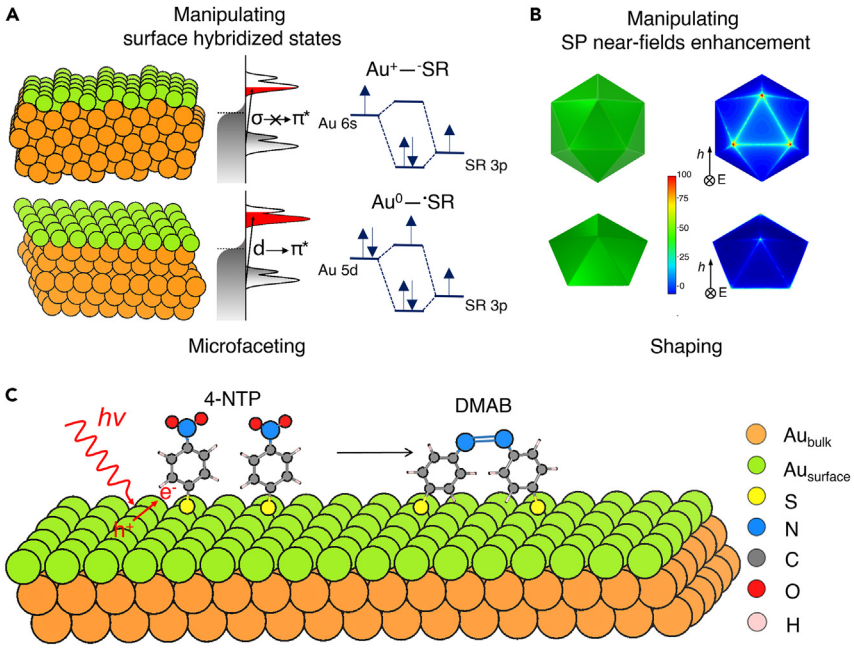

Figure 1. Schematic illustration of microscopic strategy to manipulate hot-carrier-mediated plasmonic enhancement pathways

(A) Pathway I, manipulating surface hybridized states of hybrid plasmonic nanostructures through microfaceting and associated diagram of hot-carrier generation (denoted for equant-shaped but diverse-faceted gold nanostructures, SC-NRs and PT-NRs).

(B) Pathway II, manipulating SP near-fields enhancement of hybrid plasmonic nanostructures through shaping and associated anisotropic distributions of SP near-fields (denoted for equant-faceted but diverse-shaped ones, IC-NPs and DE-NPs). The spatial distribution of SP near-fields is derived by using a 3D electromagnetic FDTD simulator with the electric field component of plane wave perpendicular to the equivalent {111} microfacets of both IC-NPs and DE-NPs.

(C) A proof-of-concept hot-carrier-mediated and plasmonic-enhanced photochemical model reaction over a plasmonic-metal/molecule hybrid system (i.e., dimerization of 4-nitrothiophenol [4-NTP] to 4,4′-dimercaptoazobenzene [DMAB]).

To this end, we propose a general strategy to regulate the direct interfacial hot-carrier transfer in hybrid plasmonic nanostructures by microfacet engineering. Microfaceting imposes additional degrees of freedom in regulating the competitive in-plane metal-metal and out-of-plane metal-adsorbate interactions over hybrid plasmonic nanostructures, thus paving new routes to manipulating metal-adsorbate-hybridized states that are associated with direct interfacial hot-carrier excitation events and efficient energy harvesting. We demonstrate this strategy in a plasmonic-metal/molecule hybrid system as a photocatalyst where microfaceting imposes a strong and direct impact on the modulation of metal-adsorbate-hybridized electronic states. A major challenge of this study lies in the decoupling of microstructural and geometric effects of plasmonic nanostructures in photocatalysis, without which the contributions from facet-dependent interfacial electronic states and geometry-dependent plasmon near-fields are totally indistinguishable. By designing and synthesizing equant-shaped but diverse-faceted gold nanostructures (i.e., single-crystal Au nanorod [SC-NR] versus penta-twinned Au NR [PT-NR]) as well as equant-faceted but diverse-shaped ones (i.e., Au icosahedron versus Au decahedron), we are able to investigate separately the respective roles of direct interfacial charge transfer and plasmon-induced local electric field enhancement in plasmon-enhanced photocatalytic coupling of 4-nitrothiophenol (4-NTP) to 4,4′-dimercaptoazobenzene (DMAB) (Figure 1).[39,40] Combining electron diffraction and electron

tomography, the three-dimensional (3D) geometry and associated microfacets of these Au nanostructures can be unambiguously elucidated. Further integrating measurements of steady-state molecular vibrational heating and associated plasmon relaxation dynamics, it is concluded that low-index microfacets feature much more efficient metal-adsorbate interfacial electronic transitions, largely retarded plasmonic relaxation and thus superior photocatalytic activity than high-index ones. The physical origin of such difference is attributed to distinct coordination numbers of these microfacets, which leads to different bonding characters of as-formed metal-adsorbate-hybridized molecular frontier states, their associated energy gap, and permissible electronic excitations. The undercoordinated Au high-index microfacet entails covalently bonded Au(I)-thiolate across the charge-polarized interface by attaining hybridized molecular frontier states with parity disallowed $\sigma \rightarrow \pi^*$ type electronic excitation, whereas the densely packed Au low-index microfacet entails nonbonded Au(0)-thiyl interaction dominated by dispersion force, thus enabling efficient parity-allowed $d \rightarrow \pi^*$ type electronic excitation.

RESULTS AND DISCUSSION

Structural design and elucidation

As a ubiquitous phenomenon, many microstructural and geometric parameters (e.g., microfacets and shapes) of nanostructures are entangled. These parameters may simultaneously impose a strong impact on the localized surface plasmonic properties of metallic nanostructures as well as the energy transfer efficiency toward an attached functional entity in a hybrid plasmonic/non-plasmonic system.[6,33] It is thus critical to figure out the decisive contribution of the plasmonic/non-plasmonic interface to the overall plasmonic-enhanced photocatalytic activity, which requires a complete physical picture of interfacial atomic structure and bonding characters as well as the underlying mechanisms of hot-carrier generation and transfer. To discriminate the respective roles of microfacet-dependent direct interfacial hot-carrier transfer and shape-dependent plasmon-induced local electric field enhancement in these plasmon-induced events, we propose a scenario for decoupling the microstructural and geometric effects by creating two separated groups of Au nanostructures with precisely controlled microfacets and shapes (Figure 1). On one side, SC-NRs and the PT-NRs are grouped together on the basis of their identical shapes and SP field distributions but distinct enclosed microfacets. On the other side, icosahedral Au nanoparticles (IC-NPs) and decahedral Au NPs (DE-NPs) are grouped together on the basis of their identical enclosed microfacets but distinct shapes and SP field distributions. In this sense, the microstructural and geometric effects are decoupled and can be investigated separately. By simple wet-chemistry strategies,[41,42] SC-NRs and PT-NRs with an identical size, shape, and aspect ratio of ~3.3 (i.e., long and short axes are ~66 and ~20 nm, respectively) were synthesized and visualized by transmission electron microscopy (TEM) (Figures S1 and S2). These NRs are expected to adopt similar anisotropic distributions of SP near-fields as verified by the finite-difference time-domain (FDTD) simulations (Figures S3A–S3D). The longitudinal SP dipolar modes of these Au NRs give rise to more intensive electric near-fields confined in the vicinity of the rod ends compared with that of the transverse SP dipolar modes. Very similar bimodal extinction bands at 520 and 710 nm associated with these transverse and longitudinal SP modes, respectively, can be observed in the UV-vis spectra for both types of NRs, which unambiguously confirms their identical shapes and plasmonic properties (Figure S4). The IC-NPs and DE-NPs are also synthesized with a similar size of ~30 nm (Figures S1 and S2) and extinction bands located at 560 and 530 nm, respectively (Figure S4).[42,43] From the TEM images, the diffraction contrast arising from the twin boundaries are clearly observed

for both types of NPs, which confirms their multiply-twinned structures. The reconstructed 3D tomograms of these NPs viewed from different projections further confirm their icosahedral and decahedral shapes (Figure S5). The IC-NPs generally have a quite spherical shape from diverse projections, whereas DE-NPs adopt a rhombic shape along an edge-on projection as observed in TEM images. Accordingly, there is a marked difference in the local electric field enhancement between these two types of polyhedral NPs according to the FDTD simulations (Figures 1, S3E, and S3F). The calculated intensities of electric near-fields for the corner, edge, and face SP modes of IC-NPs are approximately 3.4, 2.2, and 2.7 times greater than those of DE-NPs, respectively. Nevertheless, these multiply-twinned DE-NPs and IC-NPs that differ in shape from each other are well known to expose exactly identical closest-packed {111} microfacets.[44,45] For the SC-NRs and PT-NRs, the enclosed microfacets can be explicitly elucidated by uniting 3D electron tomography and nanobeam diffraction. We hereby devise a scheme that accurately registers the orientation information derived from the nanobeam diffraction over a microtome cross-section of the Au NRs with the morphological information derived from the 3D tomogram reconstructed from a tilt series of annular dark-field scanning transmission electron microscopy (ADF-STEM) images over these nanostructures (Figures 2C and 2F). The nanobeam diffraction patterns of a microtome cross-section of both SC-NRs and PT-NRs (Figures 2E and 2H) can be well indexed by the [001] zone axis of single crystalline and [011] zone axis of penta-twined face-centered cubic-structured Au, respectively, which unambiguously confirm the single-crystalline and penta-twinned nature of these NRs. By aligning the microtome cross-sections with the virtual cross-sections sliced from the reconstructed 3D tomogram of both SC-NR and PT-NR, we are able to explicitly identify the enclosed microfacets of these NRs as labeled in Figures 2D and 2G. Specifically, the rod body of SC-NR is mainly enclosed by {100} microfacets along with bridging {1k0} ($0 < k \leq 1$) ones, whereas the rod end is mainly enclosed by high-index {310} microfacets along with bridging {110} ones. On the other side, the rod body of PT-NR is mainly enclosed by {100} microfacets along with bridging {1k0} ($0 < k \leq 1$) ones as well, whereas the rod end is mainly enclosed by low-index {111} microfacets along with bridging {110} ones. The assigned microfacets can be more vividly visualized and labeled by 3D Gaussian surface curvature analysis, which permits the precise construction of the 3D structural models for both types of NRs (Figures 2A, 2B, S6, and S7). Taken together, IC-NPs and DE-NPs that differ in intensities of electric near-fields adopt identical {111} low-index microfacets, whereas the rod ends of SC-NRs and PT-NRs that exhibit identical intensities of electric near-fields adopt distinct microfacets (high index {310} versus low index {111}).

In situ kinetic study of plasmon-enhanced photocatalysis

The above structural design and elucidation of Au nanostructures provide a solid basis for decoupling the microstructural and geometric effects of hybrid plasmonic nanostructures in photocatalysis driven by direct interfacial hot electron transfer. As a proof-of-concept study, we investigate the plasmon-enhanced photocatalytic dimerization reaction over a Au/4-NTP hybrid plasmonic system by *in situ* SERS after successful thiol ligand exchange over these as-synthesized Au nanostructures (Figure S8). An incidence wavelength of 785 nm is selected to avoid the photoluminescence effects (Figure S9), which lies at the slightly longer wavelength side of the surface plasmon resonance (SPR) peak for both NPs and NRs so as to simultaneously approach the resonant condition of the highest occupied molecular orbital (HOMO)-lowest unoccupied molecular orbital (LUMO) transition of hybridized interfacial states and maintain SERS sensitivity by near-field enhancement. The proposed reaction mechanism is initiated by the photon absorption and hot electron excitation from Au surface to 4-NTP adsorbates

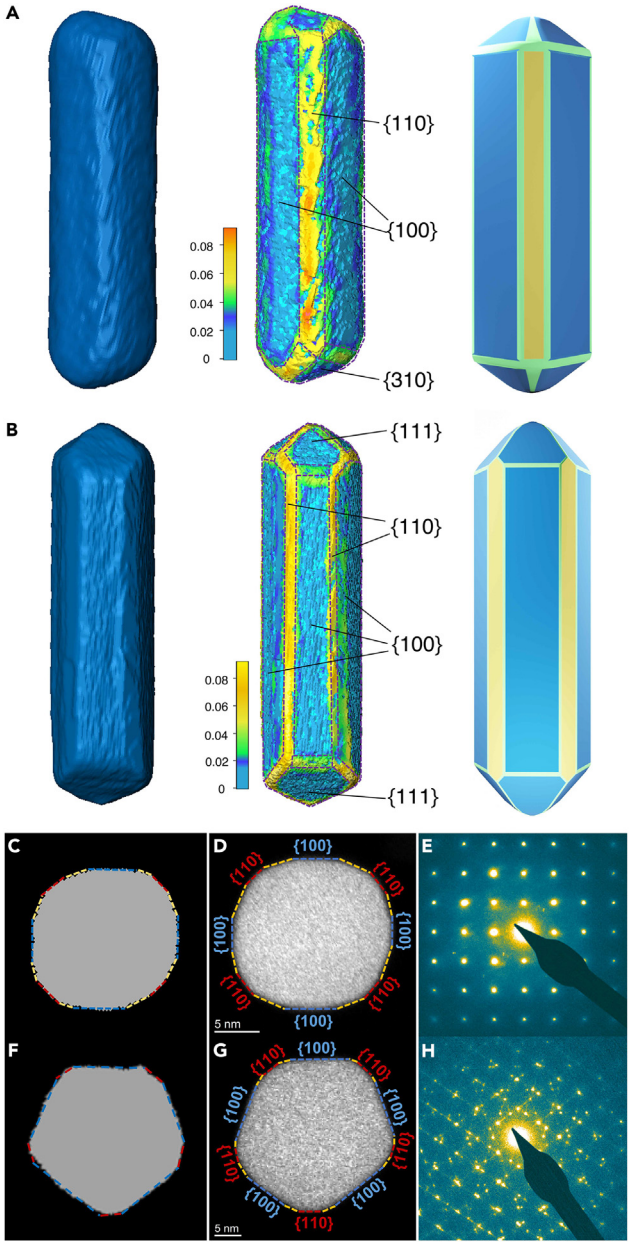

Figure 2. Three-dimensional structural elucidation and microfacets determination of Au nanorods

(A and B) From left to right, volume rendering of 3D tomogram, isosurfaces of Gaussian curvature and 3D structural model rendered in false color for (A) SC-NRs and (B) PT-NRs, respectively. {110}, {100}, {310}, and {111} microfacets are labeled on the isosurfaces of Gaussian curvature representation and highlighted in the 3D structural model.

(C–H) Cross-section ortho-slices of reconstructed 3D tomograms, high-resolution scanning transmission electron microscopy (HRSTEM) image of microtome cross-sections of Au NRs with enclosed microfacets marked by diverse colors (yellow for {1k0} [0 < k < 1] high-index microfacets) and nanobeam diffraction patterns of these microtome cross-sections for (C)–(E) SC-NRs and (F)–(H) PT-NRs.

and followed by multiple consecutive photon absorption, protonation, and dehydration steps. These photocatalytic reaction steps lead to the formation of two key intermediates nitroso-benzenethiol and hydroxyl-aminobenzenethiol, which are subject to a coupling reaction toward the formation of azoxy-benzenethiol. After two more electron

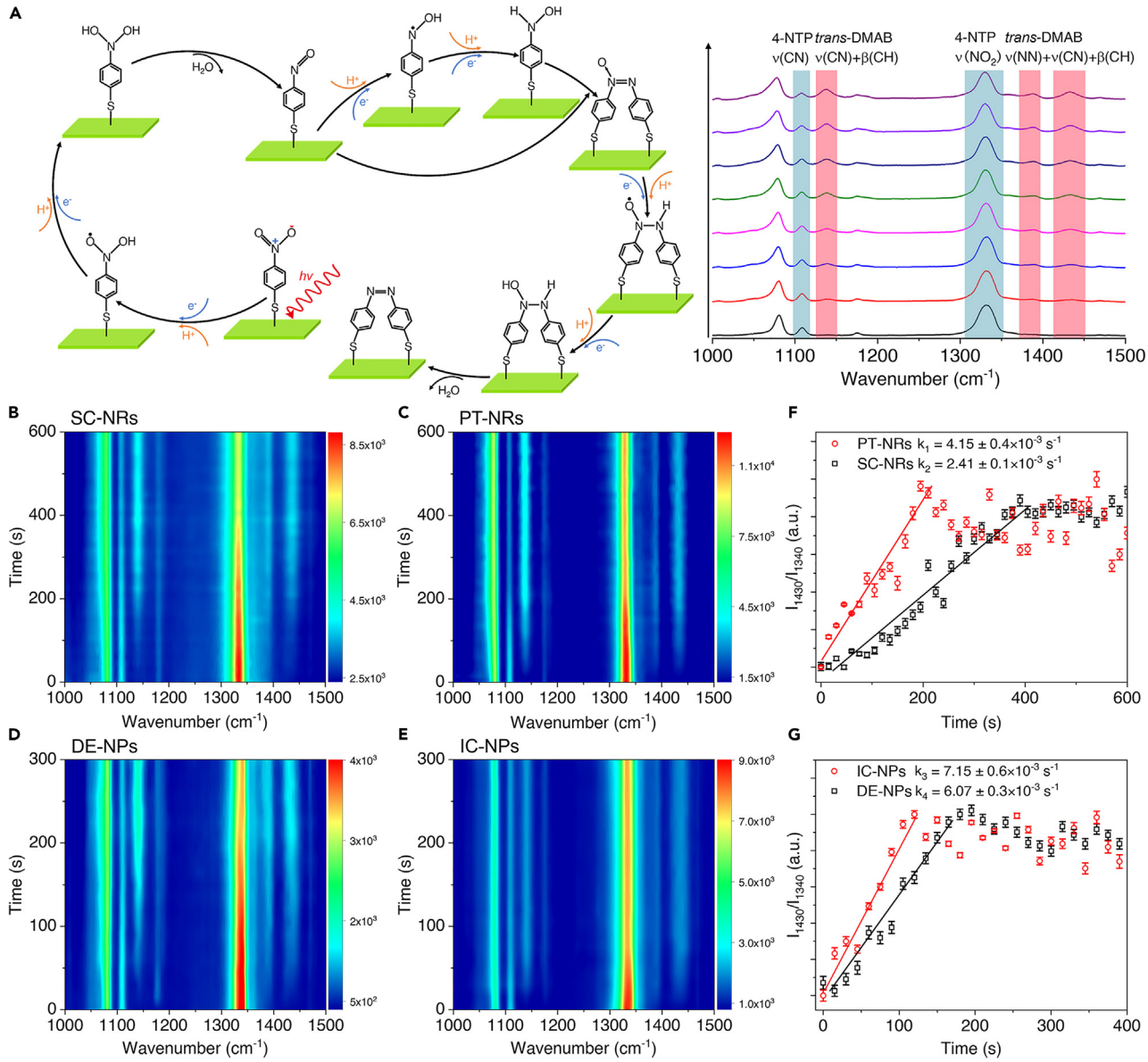

Figure 3. Quantitative kinetic measurements of hot-carrier-mediated photochemical dimerization reaction over a plasmonic-metal/molecule hybrid system by *in situ* SERS

(A) (Left) Schematic diagram of proposed plasmonic-enhanced reaction mechanism of the coupling of 4-nitrothiophenol (4-NTP) to 4,4′-dimercaptoazobenzene (DMAB). (Right) The evolving characteristic Raman bands of PT-NRs are highlighted for 4-NTP and DMAB molecules, representing the reactant and product, respectively, with a time interval of 45 s.

(B–E) 2D map of surface reaction time-series Raman spectra monitored by *in situ* SERS measurements over hybrid plasmonic systems involving (B) SC-NRs, (C) PT-NRs, (D) DE-NPs, and (E) IC-NPs, respectively.

(F and G) The extracted and fitted surface reaction kinetic parameters over these hybrid plasmonic systems.

injection steps, the final product DMAB is generated (Figures 3A and S10).[46,47] The aggregation of nanocrystals is uniformly distributed on the substrate, and the intensities of Raman bands are similar among randomly chosen probe positions (Figure S11). As shown in Figure 3B, the chemical reaction rates can be monitored from the intensity evolutions of characteristic vibrational bands in SERS spectra for both 4-NTP reactant and its dimerization product DMAB. Accordingly, by comparing the photocatalytic activities between IC-NPs and DE-NPs, the contribution of plasmonic near-field enhancement

arising from the shape effect of these Au nanostructures can be well discriminated from the contribution of CID energy transfer channel arising from their microfaceting effects. Although increased catalytic activity due to near-field enhancement effects cannot be completely ruled out, it is anticipated to have a relatively minor impact when compared with the pivotal role of microfacets. In contrast, the photocatalytic contribution of microfaceting effects can be discriminated from the contribution of shape effects by comparing the activities between SC-NRs and PT-NRs. Based on the time-series SERS spectra as shown in Figures 3B–3E, the reaction rates over different hybrid plasmonic nanostructures are quantitatively evaluated based on the diminishing characteristic vibrational bands for 4-NTP and increasing ones for DMAB, which follows a second-order reaction kinetics according to Equation S3 (details in supplemental information). The more rapid consumption of 4-NTP reactants over PT-NRs in contrast to SC-NRs entails higher photocatalytic activity of PT-NRs than that of SC-NRs (Figures 3B and 3C). The reaction rate constant of PT-NRs (k_1 = 4.15 × 10^{-3} s^{-1}) derived by fitting the time-dependent intensity ratios of Raman band at 1,432 cm^{-1} over that at 1,330 cm^{-1} is almost twice as high as that of SC-NRs (k_2 = 2.41 × 10^{-3} s^{-1}). To investigate the microstructural stability of PT-NRs, a comparison was made between the reconstructed 3D tomograms before and after photocatalysis. The results revealed that these NRs maintained an identical shape and preserved their enclosed microfacets throughout the reaction (Figure S12). As the incidence wavelength is close to the resonant wavelength of longitudinal SP dipolar mode of these Au NRs, the SERS signals are dominated by those coming from the surface reaction at rod ends.[48] Given that the two types of Au NRs exhibit very similar shapes as well as the SPR near-fields distributions, the observed marked difference in photocatalytic activity mainly arises from their distinct microfacets at rod ends. The low-index {111} microfacets at the rod ends of PT-NRs allow more efficient photon energy harnessing than the high-index {310} microfacets at the rod ends of SC-NRs. The distinct bonding characteristics of these two types of microfacets with thiol adsorbates account for such difference in photocatalytic activities, which originates from the regulated hybridized interfacial states and associated direct interfacial hot electron transfer efficiency. On the other side, we observe a minor difference in photocatalytic activity between DE-NPs and IC-NPs enclosed by identical {111} microfacets. The IC-NPs that adopt stronger SPR near-fields according to FDTD simulations (Figure S3) are slightly more reactive than DE-NPs with their respective reaction rate constants of k_3 = 7.15 × 10^{-3} s^{-1} and k_4 = 6.07 × 10^{-3} s^{-1} (Figures 3D, 3E, and 3G). It indicates that the SPR near-field enhancement plays a minor role in promoting the photocatalytic dimerization reaction over these NPs, as the excitation wavelength (785 nm) is far from their SPR resonant conditions. Accordingly, direct hot electron transfer between hybridized interfacial states formed by chemically bonded thiol adsorbates on Au {111} microfacets dominates in photocatalysis over these NPs. Notably, the microfacets at rod ends of Au NRs are generally less reactive than the {111} microfacets in Au NPs (Figures 3F and 3G), arising from wavelength-dependent competition between photochemical and photothermal effects (Figures S3 and S13). Taken together, we corroborate that microfaceting is a new and efficient route for regulating direct hot electron transfer and hot-electron-induced photochemical reactions. Notably, incomplete conversion of reactants is observed and possibly arises from competitive hot electron scavenging of oxygen, the lack of hole scavengers, and the steric hindrance effects at lower coverage of reactants.[49,50]

Mechanistic insights into hot-carrier transfer and dynamics

To provide experimentally mechanistic insights into the efficiency of hot-carrier energy extraction across the metal/adsorbate interface in these hybrid plasmonic Au nanostructures, we performed steady-state anti-Stokes and Stokes Raman spectroscopy (Figure 4). The intensities of anti-Stokes and Stokes background and Raman

bands can be extracted to evaluate the heating effects of the Au nanostructures owing to hot electron thermalization and the vibrationally excited hot adsorbates owing to the metal-adsorbate interfacial hot electron transfer, respectively.[30,31] Specifically, energetic electron and hole pairs are generated by plasmon dephasing in Landau damping formed and then thermalizes to a hot Fermi-Dirac distribution that leads to the local heating of NPs. Accordingly, the local temperature of Au nanostructures can be measured by fitting the anti-Stokes Raman background signal to the Fermi-Dirac distribution function derived from Equation S7. On the other side, the vibrational temperatures of adsorbates are calculated through ratios of the anti-Stokes to Stokes Raman intensities based on the Boltzmann distribution Equation S8 (Figures 4A–4D), arising from the injection of hot electrons via either indirect route for those attaining sufficient energy before thermalizing to equilibrium or direct route for those excited between hybridized states respectively. As shown in Figure 4F, all Au nanostructures exhibit elevated temperatures in the range of 314.7∼337.1 K with respect to the environment (298 K) upon laser irradiation as measured from anti-Stokes background (details in Figure S14 and Equations S5–S7). It is observed that both types of Au NRs and Au NPs exhibit similar local temperatures (330.5 and 337.1 K for SC-NRs and PT-NRs; 319.9 and 314.7 K for IC-NPs and DE-NPs). The Au NRs are generally heated more than Au NPs, possibly arising from the greater contribution from the Landau damping channel and associated hot electron thermalization. The vibrational temperatures of 4-NTP adsorbates are calculated from anti-Stokes and Stokes Raman intensities of vibrational modes at 330, 725, and 1,085 cm^{-1}, respectively (Figures 4B–4E). Remarkable hot electron transfer across the metal/adsorbate interface is characterized by the elevated anti-Stokes Raman bands under the 785 nm laser excitation, which is not observed under 532 nm excitation (Figure S15). The calculated vibrational temperatures of 4-NTP adsorbates are significantly elevated with respect to Au nanostructures under the 785 nm excitation (Figure 4F), whereas there lacks a considerable metal/adsorbate temperature difference characterized for hot electron transfer under the 532 nm excitation (Figure S16). Provided that the 532 nm excitation is close to the (transverse) SP dipolar modes for (Au NRs) Au NPs, the elevated vibrational temperatures of 4-NTP adsorbates over Au nanostructures at 785 nm off-resonant excitation mainly stem from the CID channel and highly efficient direct hot electron transfer across the metal/adsorbate interface. In addition, the more pronounced vibrational heating of adsorbates over PT-NRs, IC-NPs, and DE-NPs in contrast to SC-NRs is observed, which indicates higher energy transfer efficiency over these Au nanostructures where the active sites for photocatalysis are dictated by low-index {111} microfacets rather than the high-index {310} ones. As typical fingerprints of CID effects, the line broadenings of SPR peaks of extinction spectra for these hybrid plasmonic nanostructures are also evaluated (Figure S17; supplemental information). After ligand exchange with thiol adsorbates, the full width at half-maximum (FWHM) of respective SPR peaks for PT-NRs, DE-NPs, and IC-NPs based hybrid plasmonic nanostructures are significantly broadened in contrast to that for SC-NRs based one (Figure 4F), entailing the critical role of low-index {111} microfacets in promoting the direct interfacial hot electron transfer.

Actually, the hot electron dynamics of the hybrid adsorbate/metal system are also significantly modulated by the interfacial hot electron transfer mechanism, which can be directly characterized by ultrafast TA spectroscopy based on a pump-probe method. With an excitation wavelength at the summit of the transverse extinction peaks, two ground state bleach (GSB) bands centered at 550 and 750 nm are observed in the TA 2D maps of both PT-NRs and SC-NRs, which are attributed to the depletion of plasmonic electrons of the transverse and longitudinal SP

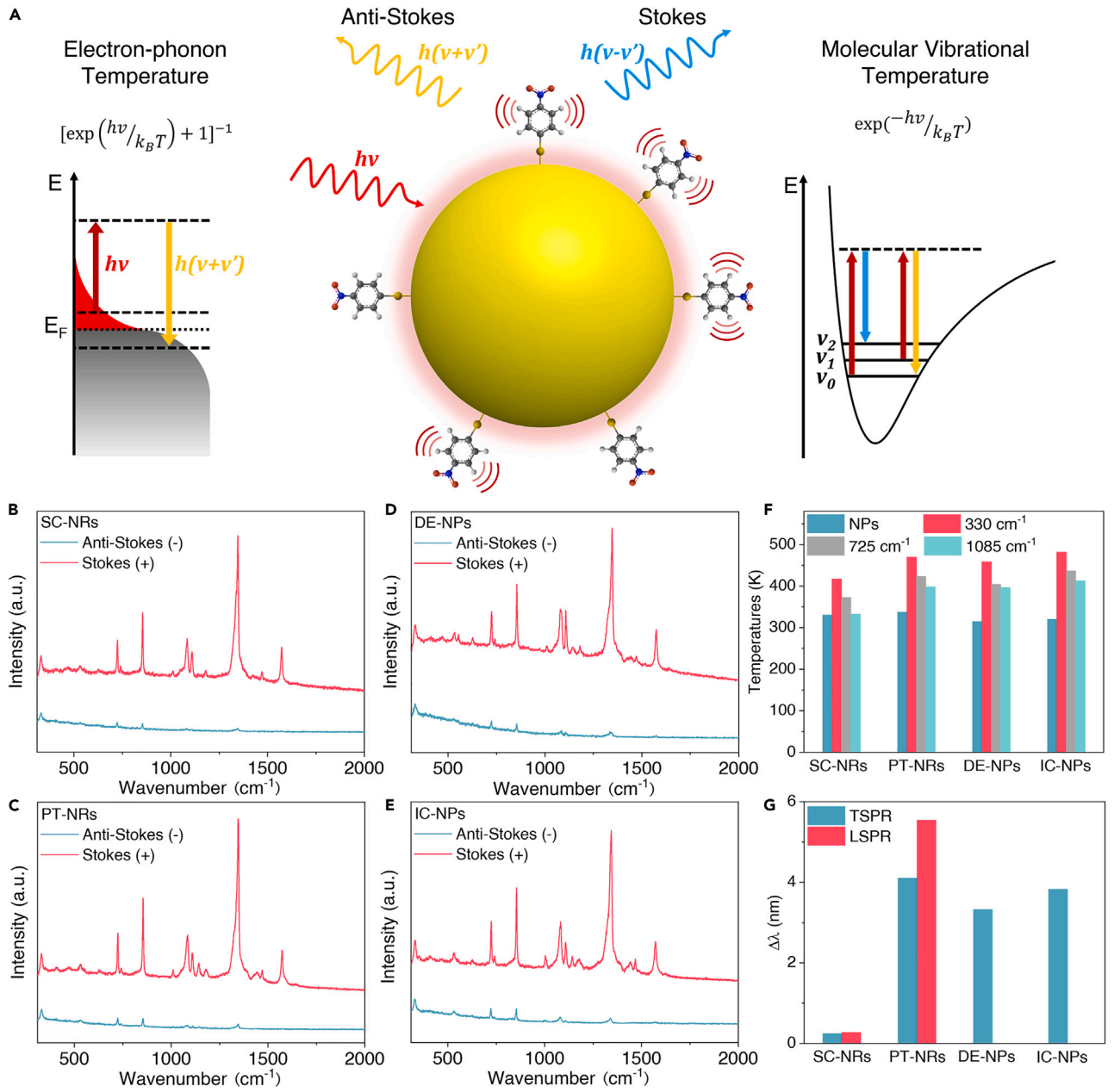

Figure 4. Quantitative measurement of steady-state hot-carrier-mediated local heating and vibrational heating effects for plasmonic nanostructures and adsorbed molecules

(A) Schematic illustration of electron-phonon temperature of plasmonic nanostructures and molecular vibrational temperature of adsorbates via combined Stokes and anti-Stokes Raman spectra.

(B–E) The steady-state Stokes and anti-Stokes Raman spectra measured over (B) SC-NRs, (C) PT-NRs, (D) DE-NPs, and (E) IC-NPs under the excitation of 785 nm.

(F) Calculated electron-phonon and molecular vibrational temperatures for Au nanoparticles and associated 4-NTP adsorbates based on their characteristic vibrational modes at 330, 725, and 1,085 cm^{-1} under the excitation of 785 nm. Temperatures of 469.8 (at 330 cm^{-1}), 423.3 (at 725 cm^{-1}), and 398 K (at 1,085 cm^{-1}) were recorded for PT-NRs. IC-NPs exhibited temperatures of 481.6 (at 330 cm^{-1}), 436.4 (at 725 cm^{-1}), and 412.9 K (at 1,085 cm^{-1}). DE-NPs showed temperatures of 458.1 (at 330 cm^{-1}), 403.7 (at 725 cm^{-1}), and 396.5 K (at 1,085 cm^{-1}). These values contrast with SC-NRs temperatures of 417 (at 330 cm^{-1}), 372.6 (at 725 cm^{-1}), and 332.3 K (at 1,085 cm^{-1}).

(G) The measured line width broadening (Δλ) based on the FWHM of the SPR peak in the extinction spectra over these Au nanoparticles after ligand exchange.

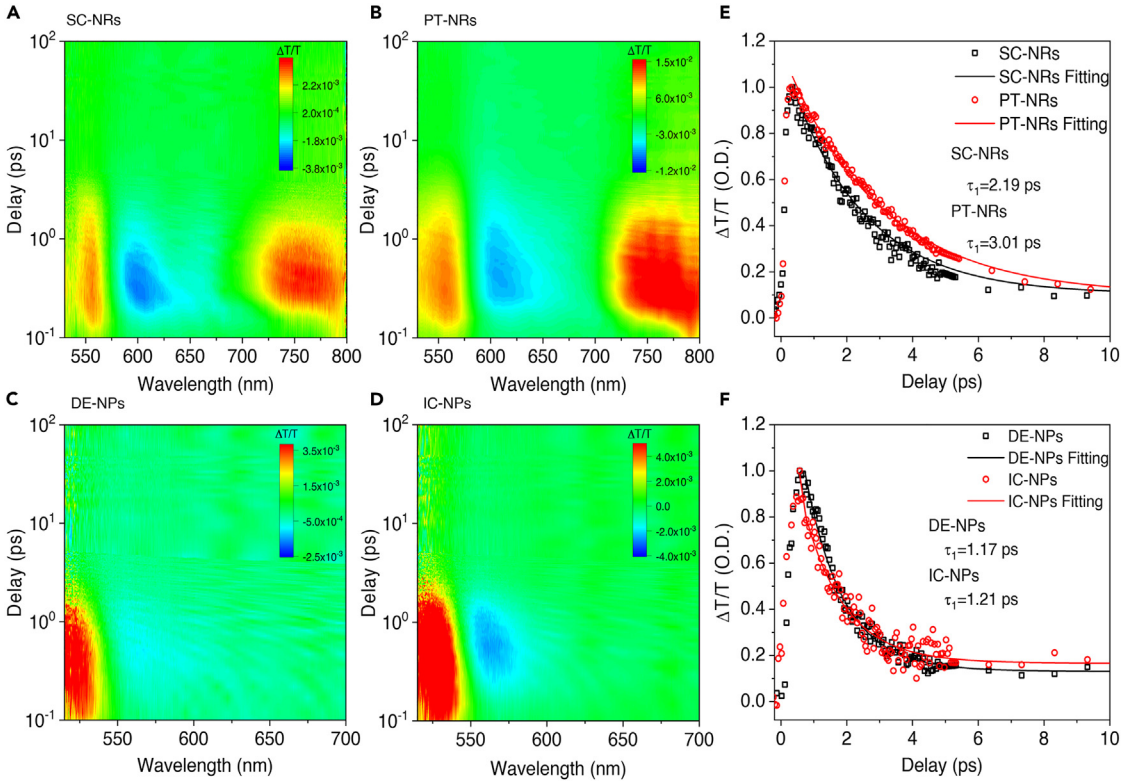

Figure 5. Hot-carrier dynamics probed by transient absorption spectroscopy

(A–D) Two-dimensional false-color plot of transient absorption (TA) spectra for (A) SC-NRs, (B) PT-NRs, (C) DE-NPs, and (D) IC-NPs under the excitation of 530 nm.

(E and F) Traces of bleach kinetics and corresponding fitted curves for (E) longitudinal SP mode of SC-NRs and PT-NRs (750 nm), and (F) SP mode of DE-NPs and IC-NPs (525 nm).

modes of these Au NRs, respectively (Figures 5A and 5B). The plasmonic bleach recovery time profiles probed at longitudinal SP modes GSB bands are visualized in Figures 5E and S18, which can be well fitted by bi-exponential functions attributed to e-ph coupling and heat dissipation into environment through phonon-media (ph-m) coupling, respectively. The fitted lifetimes of relaxation processes for longitudinal SP mode are $\tau_{e\text{-}ph}$ = 3.01/2.19 ps and $\tau_{ph\text{-}m}$ = 318.59/314.27 ps for PT-NRs and SC-NRs, respectively. The direct hot electron transfer mechanism allows the creation of vibrationally excited hot adsorbates as transient energy reservoirs and significantly retards the overall hot electron thermalization through the back-and-forth energy transfer between the metal and adsorbates repeatedly.[20,34] The prolonged hot electron thermalization time over PT-NRs with respect to SC-NRs further corroborates the superior direct hot electron transfer efficiency over the low-index {111} microfacets at the rod ends of PT-NRs. As for DE-NPs and IC-NPs that attain identical {111} microfacets, they exhibit quite similar hot electron dynamics from the GSB band at 530 nm (Figures 5C and 5D), of which the fitted relaxation lifetimes are $\tau_{e\text{-}ph}$ = 1.17/1.21 ps and $\tau_{ph\text{-}m}$ = 204.85/352.05 ps, respectively (Figure 5F).

Interfacial hybridized electronic states and excitations

To explicitly figure out the physical origin of the microfaceting effects, further insights into the nature of microfacet-dependent metal-adsorbate chemical bonding and interfacial hybridized electronic states are provided by density functional

theory (DFT) calculations (details in the supplemental information). Basically, there is an inherent competition between two pairs of interactions over the microfacets of hybrid plasmonic nanostructures, the in-plane metal–metal bonding and out-of-plane metal–adsorbate bonding. Diverse microfacets differ from each other in coordination environment and packing density of metal atoms and thus provide additional degree(s) of freedom in regulating these two types of interactions. This strategy is particularly important for noble metals such as gold, of which the $d^{10}s^1$ configuration entails the following two distinct bonding scenarios with thiol adsorbates: (1) Au–S-bonded interaction mainly contributed by *6s* valence orbitals and produces Au(I)-thiolates species and (2) Au–S-nonbonded interaction (i.e., aurophilic interaction) dominated by closed-shell *5d* valence orbitals and produces Au(0)-thiyl species (Figure 1).[51] Because the Au–Au metallic bonding is contributed by *6s*-*6s* character, it is possible to select between these two distinct Au–thiol-bonding scenarios; thus, the hybridized interfacial states by tailoring the surface packing density of Au microfacets. Specifically, the low-index Au {111} microfacets are closest packed with strongest in-plane Au–Au *6s*-*6s* bonding, which favors the nonbonded Au-S interaction in the Au-thiol hybrid system. In contrast, the loosely packed Au {310} microfacets favor the bonded Au-S interaction with more contributions from *6s* valence orbitals. By extensively investigating different adsorption configurations over both types of microfacets (Figure S19), we figure out the most thermodynamically stable adsorption geometries of 4-NTP adsorbates over the low-index {111} and high-index {310} microfacets are standing-up configuration on the 3-fold hollow sites of {111} surface and flat-lying configuration on the 2-fold bridging sites of the {310} surface, respectively (Figures 6A and 6C). As expected, the thiol adsorbate binds more strongly with the {310} microfacet with a binding energy of 3.2 eV than the {111} microfacet with a binding energy of 2.0 eV. It results in distinct metal-adsorbate interfacial hybridizations that can be clearly visualized by the projected density of states (PDOS) near the Fermi level (Figures 6B and 6D) and the spatial distributions of associated frontier molecular orbitals (MOs) of Au-S active sites as shown in (Figures 6E and 6F). Apparently, the Au {310} microfacets exhibit very strong bonded-type interfacial hybridization between Au *5d*/*6s* and S sp^2 valence states, characterized by very broad PDOS distributions. Such hybridization creates an energy gap of 1.22∼1.48 eV with a significant contribution from Au *6s* states for both occupied and unoccupied states. As a result, there is remarkable charge transfer and bond polarization observed across the Au-thiol interface from the charge density difference maps from both top and side views (Figure 6G), which validates the Au(I)-thiolate as the descriptor for the interaction between 4-NTP adsorbates and Au {310} microfacets. Specifically, by further investigating the spatial distributions of frontier MOs (Figures 6F and S20), it is concluded that the two occupied states at −1.13 (H′-2) and −0.28 eV (H′-1), respectively, are composed of Au–Au bonded states with significant *s*-*d* hybridization and Au–S bonded states formed by Au *s*-d_z^2 and S sp^2 orbital overlap with σ-type bonding characters. There are 2 weak and flat unoccupied states located at 0.09 eV (L′-1) and 0.35 eV (L′-2), which mainly arise from the Au–Au *6s*-*6s* antibonding interaction and the overlap between Au d_{xz} and 4-NTP π* orbitals with π-type antibonding characters (Figures 6D and 6F). On the contrary, the closest-packed Au {111} microfacets exhibit nonbonded interaction with 4-NTP adsorbates through closed-shell *5d* orbitals via strong van der Waals interaction (i.e., aurophilic interaction), as the Au *6s* valence states are predominantly involved in forming the in-plane Au–Au bonding. Such interfacial hybridization results in narrow PDOS distributions for highly localized and nonbonded Au *5d* and S sp^2 orbitals within both occupied and unoccupied energy range near Fermi level and opens an energy gap of 0.83∼1.88 eV. Accordingly, there lacks considerable

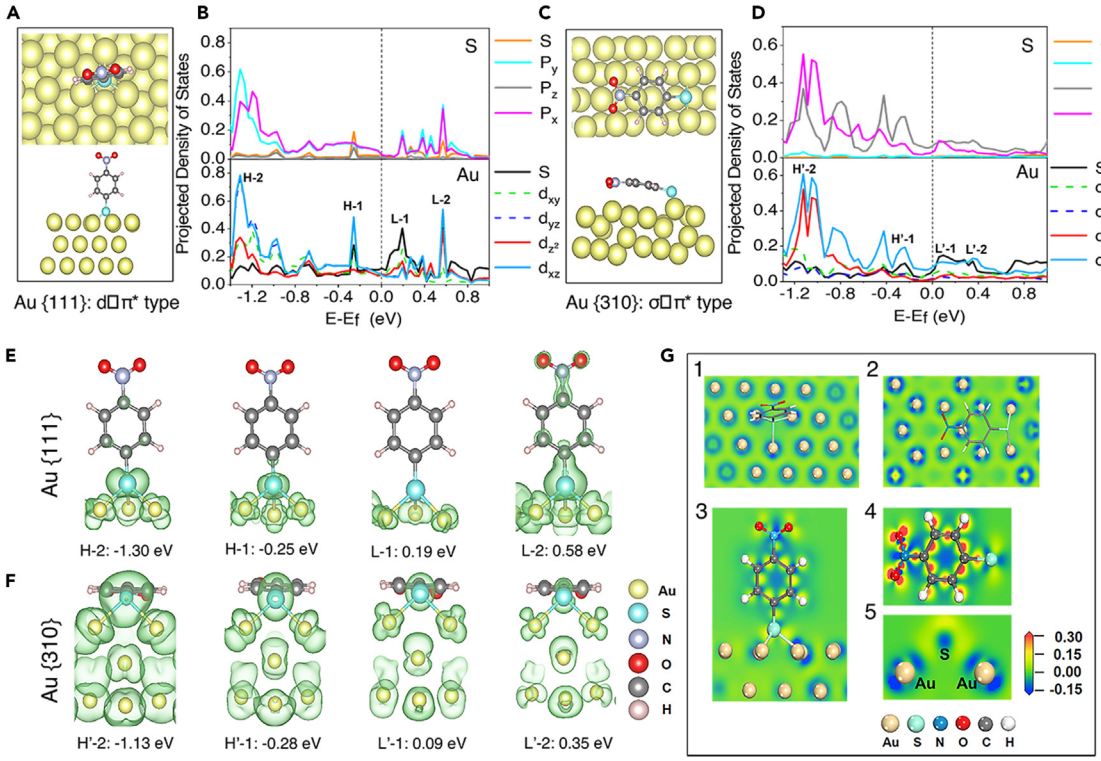

Figure 6. Theoretical calculation of metal-adsorbate interfacial hybridized electronic states

(A–D) Optimized geometries and associated PDOS for *p* states of S atom (upper) and *d* states of Au atoms underneath (lower) of hybrid systems composed of 4-NTP molecule adsorbed on (A and B) low-index {111} and (C and D) high-index {310} microfacets of Au by DFT methods. Fermi levels are marked by dashed lines.

(E and F) The spatial distribution of frontier molecular orbitals of the metal-adsorbate systems for (E) Au {111} and (F) Au {310} microfacets.

(G) The charge density difference maps of 4-NTP molecule adsorbed on (1, 3) Au {111} and (2, 4, 5) Au {310} microfacets from top and side views, respectively. The blue and orange colors represent charge depletion and accumulation regions.

bond polarization across the Au-thiol interface, and only a small fraction of charge transfer is observed in the charge density difference maps (Figure 6G), entailing the Au(0)-thiyl as the descriptor for the interaction between 4-NTP adsorbates and Au {111} microfacets. As shown in the spatial distributions of frontier MOs (Figures 6E and S20) and PDOS distributions (Figure 6B), besides the contributions from Au–Au *6s-6s* bonding, the occupied states at −1.3 eV (H-2) are composed of nonbonded Au *5d* orbitals and a fraction of σ-type orbital overlap between Au *s*-d_{z^2} and S sp^2. The occupied states at −0.25 eV (H-1) with very narrow PDOS distributions are attributed to highly localized nonbonded Au *5d* orbitals and S sp^2 radical orbitals that can be passivated through S-Au-S super-exchange effects.[51] The unoccupied states at 0.19 eV (L-1) are assigned to the Au–Au *6s-6s* antibonding interaction and those at 0.58 eV (L-2) are contributed by overlapped Au d_{xz} and 4-NTP π* orbitals (Figures 6B and 6E). Taken together, the two types of Au microfacets, i.e., the low index {111} and high index {310}, create totally different types of adsorbates (i.e., Au(0)-thiyl and Au(I)-thiolate) through nonbonded and bonded interactions, respectively. Their associated metal-centered and adsorbate-centered interfacial hybridized states that open small energy gaps enable the direct hot electron transfer process under off-resonant conditions of SP modes and across the metal-adsorbate interface, which imposes a great impact on the light-driven photochemical reactions. The undercoordinated Au high-index {310} microfacets hybridize strongly with the thiol adsorbates, which entails quite a

low density of unoccupied states and parity disallowed $\sigma \rightarrow \pi^*$ type electronic excitation. On the contrary, the densely packed Au low-index {111} microfacets bind thiol adsorbates by strong dispersion forces, which entails high densities of both occupied and unoccupied states and at the same time enables efficient parity-allowed $d \rightarrow \pi^*$ type electronic excitation. As a result, mediated by more efficient direct hot electron transfer, the hybrid plasmonic nanostructures enclosed by {111} microfacets as active sites convert adsorbates more rapidly under light irradiation.

In summary, traditional plasmonic nanotechnology has opened an avenue toward photon energy confinement and spectral fingerprint regulation by rationally designing and synthesizing plasmonic nanostructures with optimized size, shape, composition, and dielectric environment. This work has paved a new route for manipulating the pathways of hot-carrier generation, transfer, and utilization within hybrid plasmonic nanostructures through microfaceting, by providing both the precise microstructural elucidation and underlying mechanistic insights into the hot-carrier-driven photochemical reactions. These findings evoke new possibilities in harvesting more efficiently the confined photon energy within a plasmonic nanostructure across an interface formed with another non-plasmonic functional entity through nanostructure engineering.

EXPERIMENTAL PROCEDURES

Resource availability

Lead contact

Further information and requests for resources should be directed to and will be fulfilled by the lead contact, Yihan Zhu (yihanzhu@zjut.edu.cn).

Materials availability

This study did not generate new unique reagents.

Data and code availability

This study did not generate any datasets.

SUPPLEMENTAL INFORMATION

Supplemental information can be found online at https://doi.org/10.1016/j.joule.2023.11.004.

ACKNOWLEDGMENTS

This work was financially supported by the National Key Research and Development Program of China (2022YFE0113800), the National Natural Science Foundation of China (22122505 and 22075250), and the Zhejiang Provincial Natural Science Foundation of China (LR18B030003). The authors gratefully acknowledge the support provided by Professor Yu Han, King Abdullah University of Science & Technology.

AUTHOR CONTRIBUTIONS

W.S., X. Li, and Y.Z. conceived the experiments. W.S., W.Z., Q.P., and H.S. conducted synthesis and characterization. X.X. performed the simulation. W.Z., Q.P., and J.Z. performed the photocatalysis experiments. Z.W., C.Z., Y.H., and T.S. performed the ultramicrotomy, electron tomography, diffraction, and imaging experiments. W.T. and H.Z. performed the TA spectroscopy experiments. X. Liu and P.-H.T. performed the Stokes and anti-Stokes Raman spectroscopy experiments. Y.Z., W.S., and F.L. prepared the manuscript.

DECLARATION OF INTERESTS

The authors declare no competing interests.

Received: March 23, 2023
Revised: August 28, 2023
Accepted: November 3, 2023
Published: November 29, 2023

REFERENCES

1. Halas, N.J., Lal, S., Chang, W.S., Link, S., and Nordlander, P. (2011). Plasmons in strongly coupled metallic nanostructures. Chem. Rev. *111*, 3913–3961.

2. Zhang, Q.F., Hernandez, T., Smith, K.W., Jebeli, S.A.H., Dai, A.X., Warning, L., Baiyasi, R., McCarthy, L.A., Guo, H., Chen, D.H., et al. (2019). Unraveling the origin of chirality from plasmonic nanoparticle-protein complexes. Science *365*, 1475–1478.

3. Pérez-Juste, J., Pastoriza-Santos, I., Liz-Marzán, L.M., and Mulvaney, P. (2005). Gold nanorods: synthesis, characterization and applications. Coord. Chem. Rev. *249*, 1870–1901.

4. Jain, P.K., Huang, X., El-Sayed, I.H., and El-Sayed, M.A. (2008). Noble metals on the nanoscale: optical and photothermal properties and some applications in imaging, sensing, biology, and medicine. Acc. Chem. Res. *41*, 1578–1586.

5. Huang, X., Li, S.Z., Huang, Y.Z., Wu, S.X., Zhou, X.Z., Li, S.Z., Gan, C.L., Boey, F., Mirkin, C.A., and Zhang, H. (2011). Synthesis of hexagonal close-packed gold nanostructures. Nat. Commun. *2*, 292.

6. Zhang, Y.C., He, S., Guo, W.X., Hu, Y., Huang, J.W., Mulcahy, J.R., and Wei, W.D. (2018). Surface-plasmon-driven hot electron photochemistry. Chem. Rev. *118*, 2927–2954.

7. Brongersma, M.L., Halas, N.J., and Nordlander, P. (2015). Plasmon-induced hot carrier science and technology. Nat. Nanotechnol. *10*, 25–34.

8. Jauffred, L., Samadi, A., Klingberg, H., Bendix, P.M., and Oddershede, L.B. (2019). Plasmonic heating of nanostructures. Chem. Rev. *119*, 8087–8130.

9. Fan, W.P., Yung, B., Huang, P., and Chen, X.Y. (2017). Nanotechnology for multimodal synergistic cancer therapy. Chem. Rev. *117*, 13566–13638.

10. Lin, K.Q., Yi, J., Zhong, J.H., Hu, S., Liu, B.J., Liu, J.Y., Zong, C., Lei, Z.C., Wang, X., Aizpurua, J., et al. (2017). Plasmonic photoluminescence for recovering native chemical information from surface-enhanced Raman scattering. Nat. Commun. *8*, 14891.

11. Bowen, A.M., Motala, M.J., Lucas, J.M., Gupta, S., Baca, A.J., Mihi, A., Alivisatos, A.P., Braun, P.V., and Nuzzo, R.G. (2012). Triangular elastomeric stamps for optical applications: near-field phase shift photolithography, 3D proximity field patterning, embossed antireflective coatings, and SERS sensing. Adv. Funct. Mater. *22*, 2927–2938.

12. Chen, C., Li, Y., Kerman, S., Neutens, P., Willems, K., Cornelissen, S., Lagae, L., Stakenborg, T., and Van Dorpe, P. (2018). High spatial resolution nanoslit SERS for single-molecule nucleobase sensing. Nat. Commun. *9*, 1733.

13. Lee, W., Kang, B.H., Yang, H., Park, M., Kwak, J.H., Chung, T., Jeong, Y., Kim, B.K., and Jeong, K.H. (2021). Spread spectrum SERS allows label-free detection of attomolar neurotransmitters. Nat. Commun. *12*, 159.

14. Aslam, U., Rao, V.G., Chavez, S., and Linic, S. (2018). Catalytic conversion of solar to chemical energy on plasmonic metal nanostructures. Nat. Catal. *1*, 656–665.

15. Lindstrom, C.D., and Zhu, X.Y. (2006). Photoinduced electron transfer at molecule-metal interfaces. Chem. Rev. *106*, 4281–4300.

16. Cacovich, S., Vidon, G., Degani, M., Legrand, M., Gouda, L., Puel, J.-B., Vaynzof, Y., Guillemoles, J.-F., Ory, D., and Grancini, G. (2022). Imaging and quantifying non-radiative losses at 23% efficient inverted perovskite solar cells interfaces. Nat. Commun. *13*, 2868.

17. Ahlawat, M., Roy, A., and Rao, V.G. (2022). Efficient extraction of energetic charge carriers from an engineered plasmonic nanocomposite to perform cascade reactions. ChemNanoMat *8*, e202100416.

18. Guo, J., Zhang, Y., Shi, L., Zhu, Y.F., Mideksa, M.F., Hou, K., Zhao, W.S., Wang, D.W., Zhao, M.T., Zhang, X.F., et al. (2017). Boosting hot electrons in hetero-superstructures for plasmon-enhanced catalysis. J. Am. Chem. Soc. *139*, 17964–17972.

19. Wu, K., Chen, J., McBride, J.R., and Lian, T. (2015). Efficient hot-electron transfer by a plasmon-induced interfacial charge-transfer transition. Science *349*, 632–635.

20. Shao, W., Pan, Q.Q., Chen, Q.L., Zhu, C.Z., Tao, W.J., Zhu, H.M., Song, H.J., Liu, X.L., Tan, P.H., Sheng, G., et al. (2021). Symmetry breaking in monometallic nanocrystals toward broadband and direct electron transfer enhanced plasmonic photocatalysis. Adv. Funct. Mater. *31*, 2006738.

21. Govorov, A.O., Zhang, H., and Gun'ko, Y.K. (2013). Theory of photoinjection of hot plasmonic carriers from metal nanostructures into semiconductors and surface molecules. J. Phys. Chem. C *117*, 16616–16631.

22. Lee, Y.K., Jung, C.H., Park, J., Seo, H., Somorjai, G.A., and Park, J.Y. (2011). Surface plasmon-driven hot electron flow probed with metal-semiconductor nanodiodes. Nano Lett. *11*, 4251–4255.

23. Li, K., Hogan, N.J., Kale, M.J., Halas, N.J., Nordlander, P., and Christopher, P. (2017). Balancing near-field enhancement, absorption, and scattering for effective antenna-reactor plasmonic photocatalysis. Nano Lett. *17*, 3710–3717.

24. Mukherjee, S., Zhou, L.A., Goodman, A.M., Large, N., Ayala-Orozco, C., Zhang, Y., Nordlander, P., and Halas, N.J. (2014). Hot-electron-induced dissociation of H-2 on gold nanoparticles supported on SiO2. J. Am. Chem. Soc. *136*, 64–67.

25. Mukherjee, S., Libisch, F., Large, N., Neumann, O., Brown, L.V., Cheng, J., Lassiter, J.B., Carter, E.A., Nordlander, P., and Halas, N.J. (2013). Hot electrons do the impossible: plasmon-induced dissociation of H-2 on Au. Nano Lett. *13*, 240–247.

26. Linic, S., Chavez, S., and Elias, R. (2021). Flow and extraction of energy and charge carriers in hybrid plasmonic nanostructures. Nat. Mater. *20*, 916–924.

27. Lee, S.A., and Link, S. (2021). Chemical interface damping of surface plasmon resonances. Acc. Chem. Res. *54*, 1950–1960.

28. Bosbach, J., Hendrich, C., Stietz, F., Vartanyan, T., and Träger, F. (2002). Ultrafast dephasing of surface plasmon excitation in silver nanoparticles: influence of particle size, shape, and chemical surrounding. Phys. Rev. Lett. *89*, 257404.

29. Hövel, H., Fritz, S., Hilger, A., Kreibig, U., and Vollmer, M. (1993). Width of cluster plasmon resonances – bulk dielectric functions and chemical interface damping. Phys. Rev. B Condens. Matter *48*, 18178–18188.

30. Boerigter, C., Campana, R., Morabito, M., and Linic, S. (2016). Evidence and implications of direct charge excitation as the dominant mechanism in plasmon-mediated photocatalysis. Nat. Commun. *7*, 10545.

31. Boerigter, C., Aslam, U., and Linic, S. (2016). Mechanism of charge transfer from plasmonic nanostructures to chemically attached materials. ACS Nano *10*, 6108–6115.

32. Furube, A., Du, L., Hara, K., Katoh, R., and Tachiya, M. (2007). Ultrafast plasmon-induced electron transfer from gold nanodots into TiO2 nanoparticles. J. Am. Chem. Soc. *129*, 14852–14853.

33. Liu, Y.W., Chen, Q.L., Cullen, D.A., Xie, Z.X., and Lian, T.Q. (2020). Efficient hot electron transfer from small au nanoparticles. Nano Lett. *20*, 4322–4329.

34. Bauer, C., Abid, J.P., and Girault, H.H. (2006). Hot adsorbate-induced retardation of the internal thermalization of nonequilibrium electrons in adsorbate-covered metal nanoparticles. J. Phys. Chem. B *110*, 4519–4523.

35. Gellé, A., Jin, T., de la Garza, L., Price, G.D., Besteiro, L.V., and Moores, A. (2020). Applications of plasmon-enhanced nanocatalysis to organic transformations. Chem. Rev. *120*, 986–1041.

36. Aruda, K.O., Tagliazucchi, M., Sweeney, C.M., Hannah, D.C., Schatz, G.C., and Weiss, E.A. (2013). Identification of parameters through which surface chemistry determines the lifetimes of hot electrons in small Au nanoparticles. Proc. Natl. Acad. Sci. USA *110*, 4212–4217.

37. Aslam, U., Chavez, S., and Linic, S. (2017). Controlling energy flow in multimetallic nanostructures for plasmonic catalysis. Nat. Nanotechnol. *12*, 1000–1005.

38. Foerster, B., Spata, V.A., Carter, E.A., Sönnichsen, C., and Link, S. (2019). Plasmon damping depends on the chemical nature of the nanoparticle interface. Sci. Adv. *5*, eaav0704.

39. Zhan, C., Chen, X.J., Yi, J., Li, J.F., Wu, D.Y., and Tian, Z.Q. (2018). From plasmon-enhanced molecular spectroscopy to plasmon-mediated chemical reactions. Nat. Rev. Chem. *2*, 216–230.

40. Wang, X., Huang, S.C., Hu, S., Yan, S., and Ren, B. (2020). Fundamental understanding and applications of plasmon-enhanced Raman spectroscopy. Nat. Rev. Phys. *2*, 253–271.

41. Ni, W.H., Kou, X., Yang, Z., and Wang, J.F. (2008). Tailoring longitudinal surface plasmon wavelengths, scattering and absorption cross sections of gold nanorods. ACS Nano *2*, 677–686.

42. Sánchez-Iglesias, A., Winckelmans, N., Altantzis, T., Bals, S., Grzelczak, M., and Liz-Marzán, L.M. (2017). High-yield seeded growth of monodisperse Pentatwinned gold nanoparticles through thermally induced seed twinning. J. Am. Chem. Soc. *139*, 107–110.

43. Kwon, K., Lee, K.Y., Lee, Y.W., Kim, M., Heo, J., Ahn, S.J., and Han, S.W. (2007). Controlled synthesis of icosahedral gold nanoparticles and their surface-enhanced Raman scattering property. J. Phys. Chem. C *111*, 1161–1165.

44. Ma, X.M., Lin, F., Chen, X., and Jin, C.H. (2020). Unveiling growth pathways of multiply twinned gold nanoparticles by in situ liquid cell transmission electron microscopy. ACS Nano *14*, 9594–9604.

45. Du, J.S.S., Zhou, W.J., Rupich, S.M., and Mirkin, C.A. (2021). Twin pathways: discerning the origins of multiply twinned colloidal nanoparticles. Angew. Chem. Int. Ed. Engl. *60*, 6858–6863.

46. Zhang, Y.S., Hu, Y.F., Li, G.K., and Zhang, R.K. (2019). A composite prepared from gold nanoparticles and a metal organic framework (type MOF-74) for determination of 4-nitrothiophenol by surface-enhanced Raman spectroscopy. Mikrochim. Acta *186*, 477.

47. Koopman, W., Sarhan, R.M., Stete, F., Schmitt, C.N.Z., and Bargheer, M. (2020). Decoding the kinetic limitations of plasmon catalysis: the case of 4-nitrothiophenol dimerization. Nanoscale *12*, 24411–24418.

48. Huang, J., Zhu, Y., Lin, M., Wang, Q., Zhao, L., Yang, Y., Yao, K.X., and Han, Y. (2013). Site-specific growth of Au–Pd alloy horns on Au nanorods: A platform for highly sensitive monitoring of catalytic reactions by surface enhancement Raman spectroscopy. J. Am. Chem. Soc. *135*, 8552–8561.

49. Christopher, P., Xin, H., and Linic, S. (2011). Visible-light-enhanced catalytic oxidation reactions on plasmonic silver nanostructures. Nat. Chem. *3*, 467–472.

50. Huang, Y.F., Zhang, M., Zhao, L.B., Feng, J.M., Wu, D.Y., Ren, B., and Tian, Z.Q. (2014). Activation of oxygen on gold and silver nanoparticles assisted by surface plasmon resonances. Angew. Chem. Int. Ed. Engl. *53*, 2353–2357.

51. Reimers, J.R., Ford, M.J., Halder, A., Ulstrup, J., and Hush, N.S. (2016). Gold surfaces and nanoparticles are protected by Au(0)-thiyl species and are destroyed when Au(I)-thiolates form. Proc. Natl. Acad. Sci. USA *113*, E1424–E1433.